

---

This is an electronic reprint of the original article.  
This reprint may differ from the original in pagination and typographic detail.

Tamminen, Aleks; Baggio, Mariangela; Nefedova, Irina; Sun, Qiushuo; Presnyakov, Semyon; Ala-laurinaho, Juha; Brown, Elliot; Wallace, Vincent; Macpherson, Emma; Maloney, Thaddeus; Kravchenko, Natalia; Salkola, Mika; Deng, Sophie; Taylor, Zachary

## Extraction of thickness and water content gradients in hydrogel-based, water-backed corneal phantoms via submillimeter wave reflectometry

*Published in:*  
IEEE Transactions on Terahertz Science and Technology

*DOI:*  
[10.1109/TTHZ.2021.3099058](https://doi.org/10.1109/TTHZ.2021.3099058)

Published: 01/11/2021

*Document Version*  
Peer-reviewed accepted author manuscript, also known as Final accepted manuscript or Post-print

*Please cite the original version:*  
Tamminen, A., Baggio, M., Nefedova, I., Sun, Q., Presnyakov, S., Ala-laurinaho, J., Brown, E., Wallace, V., Macpherson, E., Maloney, T., Kravchenko, N., Salkola, M., Deng, S., & Taylor, Z. (2021). Extraction of thickness and water content gradients in hydrogel-based, water-backed corneal phantoms via submillimeter wave reflectometry. *IEEE Transactions on Terahertz Science and Technology*, 11(6), 647-659.  
<https://doi.org/10.1109/TTHZ.2021.3099058>

---

This material is protected by copyright and other intellectual property rights, and duplication or sale of all or part of any of the repository collections is not permitted, except that material may be duplicated by you for your research use or educational purposes in electronic or print form. You must obtain permission for any other use. Electronic or print copies may not be offered, whether for sale or otherwise to anyone who is not an authorised user.

# Extraction of thickness and water content gradients in hydrogel-based, water-backed corneal phantoms via submillimeter wave reflectometry

A. Tamminen<sup>1,2</sup>, M. Baggio<sup>1,2</sup>, I. Nefedova<sup>1,2</sup>, Q. Sun<sup>3</sup>, S. Presnyakov<sup>4</sup>, J. Ala-Laurinaho<sup>1,2</sup>, E.R. Brown<sup>5</sup>, V.P. Wallace<sup>6</sup>, E. MacPherson<sup>7</sup>, T. Maloney<sup>8</sup>, N.P. Kravchenko<sup>4</sup>, M. Salkola<sup>9</sup>, S. Deng<sup>10</sup>, Z.D. Taylor<sup>1,2</sup>

**Abstract**— Absolute thickness and free water content gradients in gelatin-based corneal phantoms with physiologically accurate radii of curvature, and aqueous backing were extracted via coherent submillimeter wave reflectometry at 220–330 GHz. Fourier-domain based calibration methods, utilizing temporal and spatial gating, were developed and yielded peak-to-peak amplitude and phase clutter of  $10^{-3}$  and  $0.1^\circ$ , respectively for signal to noise ratios between 40 dB and 50 dB. Twelve phantoms were fabricated. Calibration methods enabled quantification of target sphericity that strongly correlated with optical coherence tomography-based sphericity metrics via image segmentation. Extracted free water volume fraction varied less than 5 % in the 5 phantoms whose fabrication yielded the most spherical geometry. Submillimeter wave-based thickness accuracy was better than  $111 \mu\text{m}$  ( $\sim\lambda/9$ ) with average of  $65 \mu\text{m}$  ( $\sim\lambda/17$ ) and standard deviation of  $44 \mu\text{m}$  ( $\sim\lambda/25$ ) for phantoms with physiologically relevant geometry. Monte Carlo simulations of measurement noise and uncertainty limits agree with experimental data analysis and indicates a lower thickness accuracy limit of  $33 \mu\text{m}$ , and water content sensitivities of 0.5 % and 11.8 % for the anterior and posterior segments respectively. Numerical analysis suggests measurement fidelity was SNR limited and identified optical path length ambiguities within the cornea where a continuum of thickness/water gradient pairs produce statistically insignificant differences in complex reflection coefficient for finite SNR. This is the first known submillimeter-wave measurement technique able to extract both the thickness and water content gradients from a soft-tissue phantom, with a water backing, without the need for ancillary measurements.

**Index Terms**— Corneal phantom, gelatin hydrogel, submillimeter-wave spectroscopy, optical-coherence tomography

## I. INTRODUCTION

Submillimeter-wave and THz spectroscopy are good candidates for non-contact assessment of corneal water content. The submillimeter-wave permittivity of corneal tissue is a strong function of water content. Additionally, the cornea features complex optical path lengths due to its thickness ( $0.58 \text{ mm} \rightarrow 0.53 \cdot \lambda_{275 \text{ GHz}}$ ), axial water gradients and non-trivial permittivity differential at the posterior segment-aqueous humor interface. Thus, resolution of the cornea's submillimeter wave, lossy longitudinal modes may provide early and sensitive assessment of abnormal tissue water content as it relates physiology and disease [1][2][3][4].

Significant work has been carried out to measure millimeter-wave and THz reflectivity from corneas and corneal phantoms [5], [6], [7],

Manuscript received 12 March 2021, revised 24<sup>th</sup> June 2021. A. Tamminen, M. Baggio, I. Nefedova, J. Ala-Laurinaho, and Z. D. Taylor are with Aalto University Department of Electronics and Nanoengineering, MilliLab, Espoo, Finland (phone: +358505137989, email: aleksi.tamminen@aalto.fi). Q. Sun is with University of Birmingham, School of Physics and Astronomy, Birmingham UK. E. MacPherson is with University of Warwick, Department of Physics, Coventry, UK. T. Maloney is with Aalto University, Department of Bioproducts and Biosystems, Espoo, Finland. S. Presnyakov is with National Research University Higher School of Economics, RU-101000 Moscow, Russia. N.P. Kravchenko is with National Research University Higher School of Economics, RU-101000 Moscow, Russia. E.R. Brown is with Wright State University, Department of Electrical Engineering, Dayton, OH, USA. V.P. Wallace is with University of Western Australia, School of Physics, Maths and Computing, Physics, AUS-6009 Perth, Australia. S. Deng is with University of California, Los Angeles, Department of Ophthalmology, Los Angeles, CA, USA. M. Salkola is with Revenio Oy, Vantaa, Finland

[8], [9], [10], and [11]. Some of the measurement campaigns have characterized corneal tissue reflectivity in a qualitative manner, where a transition is observed when the cornea, e.g., dries or hydrates [12], [13]. The *in vivo* measurements are easily disturbed by alignment issues due to the subject in constant movement. Thus, phantoms allow for a more static environment to evaluate corneal hydration sensing methods. Some corneal phantoms are accurately characterized, e.g., contact lenses on metal spheres with a known thickness and water content [14].

Here, we present submillimeter-wave measurements and parameter fitting for the simultaneous extraction of the absolute water content and the thickness of realistic corneal phantoms. The phantoms were backed by water with controlled pressure mimicking *in vivo* intra-ocular pressure. The presence of water backing under physiologic relevant pressure initiated water-transport phenomena, characterized by evaporation and water diffusion. These processes set up a gradient within the gelatin bulk thus further mimicking *in vivo* conditions.

Optical-coherence tomography was used in combination with submillimeter-wave reflectivity measurements to estimate phantom thickness and water content. To achieve an accurate measurement, time gating and spatial-domain filtering techniques were applied to suppress the multiple reflections present in the quasioptics. Similar techniques have been used in high-accuracy black-body calibration target characterization [15], [16], [17].

The depth dependent parameters of curved phantoms were approximated with stratified medium and Bruggeman effective medium permittivity to present the layers with varying water content similarly to well-known thin-film reflectivity [18], [19].

The measurement sensitivity of the system was explored via a Monte-Carlo analysis that simulated corneal phantom reflectivity measurements. The analysis resulted in expected root-mean-squared error (RMSE) values for the thickness and water content predictions as a function of signal-to-noise ratio (SNR). We believe that these are the first results with realistic corneal parameter extraction at submillimeter waves with complementary thickness and water-content data from OCT and DSC measurements.

In the following, we discuss the free and bound water distributions in human cornea in Section II. We present the corneal phantom in Section III, the submillimeter-wave reflectivity measurement setup in Section IV, the corneal model and parameter fitting algorithm in Section V, the experimentally determined phantom thickness and water content in Section VI and theoretical sensitivity estimation in Section VII. We finally end up with conclusion.

## II. FREE AND BOUND WATER GRADIENTS IN HUMAN CORNEA

The high total-water content in the cornea, and the tissue's robust mechanical structure indicate high bound-water content. Further, proximity to the aqueous humor suggests bound- and free-water gradients. While much work on bound-water content quantification has been published, the only known bound water gradient characterization is reported in [20]. Twenty-six bovine corneas varying from 0.75 to 0.88 mm in thickness were sectioned perpendicular to the visual axis. The total-water content and free-water content were quantified for each section using

thermogravimetric analysis and DSC. These results were recompiled and plotted in Figure 1 where the data from Figure N in [20] are labeled as Sample N. Figure 1(a) shows the total water content as a function of depth and Figure 1(b) shows bound-water content as a percent of the total water content for the same depth. Note that samples 1 – 3 were sectioned starting from the anterior while samples 4 and 5 were sectioned from the posterior.

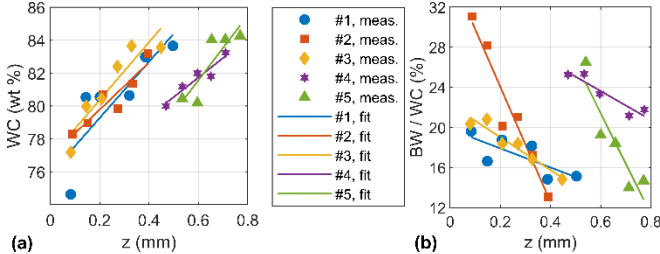


Figure 1. (a) Total-water and (b) bound-water content of ex vivo bovine cornea as a function of depth. The data is replotted from [20] and was obtained with thermogravimetric analysis and differential scanning calorimetry (DSC). Data from Ref. [20] are labeled as Samples 1 – 5 here.

The total-water content displayed in Figure 1(a) shows an average positive gradient of  $\sim 2\%/100 \mu\text{m}$  from anterior to posterior. The extrapolation of trends in samples 1 – 3 to the anterior do not coincide with the posterior section data from samples 4 and 5 demonstrating the practical difficulties of these experiments. The bound-water gradients reported in Figure 1(b) are less consistent than the total water content gradients and further show the difficulty in ascertaining bound-water content in corneal tissue. The graphs also indicate a negative gradient and overall, the presence of significant bound water ranging from 25 % to 30 % of the total water content at the anterior surface. Furthermore, the linear regression lines suggest a super-linear free water content increase as a function of depth. The significant fraction of bound water has ramifications for THz spectroscopy since the cornea has less free water than indicated in previously utilized models [21], [22]. Compared to [21] and [22]; (1) the anterior segment reflection is lower, (2) the overall optical path loss is lower, and (3) the permittivity differential at the posterior-aqueous humor interface is higher. Thus, the gelatin phantom should have significant free water content and a non-trivial, positive gradient in free water.

### III. CORNEAL PHANTOM

Figure 2(a) shows a comparison sketch of the human cornea and the corneal phantom used in this work. The human cornea median central corneal thickness (CCT) is reported to be  $540 \mu\text{m}$  [23]. Close to the optical axis, the cornea thickness is almost constant, whereas it gradually increasing towards the corneal periphery. The effect of increasing thickness in submillimeter-wave measurements can be limited by designing optics that limit the transverse extent of the Gaussian beam illumination [8]. The front and back surfaces of the phantoms were designed as concentric spherical shells to remove varying thickness as a confounder and help focus on intrinsic SNR and illumination band limits on parameter estimation. The phantom was backed by an optically thick water volume simulate the aqueous humor.

Figure 3(a) shows the mold used to fabricate the phantoms. Two molds have a nominal thickness of  $580 \mu\text{m}$  and  $680 \mu\text{m}$ . A sketch of the gelatin shell is shown in Figure 3 (b). The phantom consists of a spherical gelatin hydrogel shell backed with water volume at a pressure of  $980 \text{ Pa}$ , which approximates the intra-ocular pressure in human cornea and helps maintain phantom geometry. The mounted phantom with pressure maintenance tubes and mounting washer are

shown in Figure 3 (c). The cornea phantom's *en-face* diameter was 12 mm. Twelve (12) phantoms were fabricated for this work, six 0.58-mm thick phantoms and six 0.68-mm thick phantoms. The phantoms are labeled A – L in the order they were measured (Figure 5). The measurements alternated between 0.58-mm and 0.68-mm thick phantoms to reduce any bias between the thickness groups based on measurement time point.

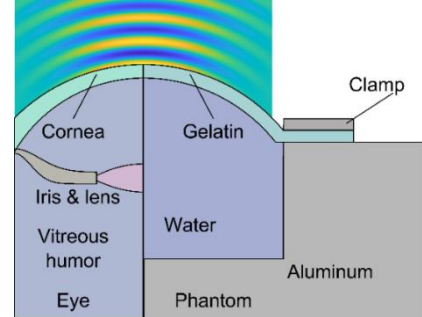


Figure 2. Sketches of the human cornea and a phantom.

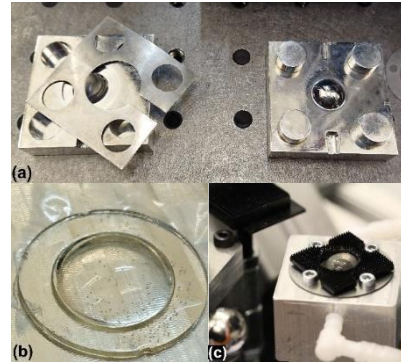


Figure 3. a) Stainless steel mold for gelatin hydrogel. Metal shims are used to create phantoms with different thickness. b) Fabricated gelatin phantom just after removal from the mold. c) Phantom installed in the holder providing realistic intra-ocular pressure. Radar absorbing material is used to suppress scattering from the high-reflectivity mount.

#### A. OCT image-based quantification of corneal phantom geometry

Optical-coherence tomography was used to quantify gelatin hydrogel phantom thickness and shape. The OCT system was a swept source, 1300-nm unit (VEG210, Thorlabs Inc.) and was used to acquire three-dimensional tomographic images prior to and following submillimeter-wave reflectivity measurements. The OCT images provided ground truth measurements of central corneal thickness, radius of curvature, and a qualitative assessment of the phantom integrity.

The OCT images of the corneal phantoms were processed with the edge detection algorithm presented in [24]. The corneal apex was identified via the central, saturated normal incidence artifact. The detected edges were smoothed and fitted to circular arcs as shown in Figure 4. Sphericity was hypothesized to correlate with CCT and CTWC estimation accuracy and the root mean square difference between the detected edges and their circular arc fits are displayed at the bottom of each panel shown in Figure 4. Healthy human cornea has RoC deviation less than  $0.1 \text{ mm}$  [25].

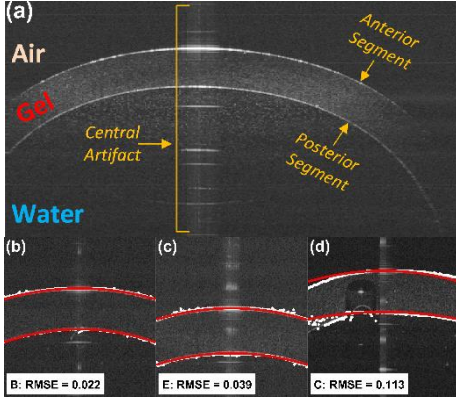


Figure 4. Examples of the corneal phantom processed with the edge detection algorithm before the submillimeter wave measurement. The OCT-derived RMSE error to a spherical surface is shown in the insets in b-d.

Submillimeter wave reflectivity measurement duration was  $\sim 60$  minutes per phantom during which the water pressure typically decreased via small water leakages through, e.g., the phantom-mount interface. Due to this pressure drop the phantom anterior surface apex moved about  $\sim 0.1$  mm throughout the measurement. The movement is partly compensated as the height of the phantom was adjusted at several points during the measurement operation. The phantom CCT and RoC were analyzed before and after the reflectivity measurements via OCT. The corneal-phantom dimensions were assumed to change linearly in time, and they were interpolated for accurate estimation at the time of submillimeter-wave measurement. Figure 5 shows OCT-derived characterization of corneal phantom thickness and anterior surface radius of curvature at different points in time during the measurements. In general, the CCT decreases with time and RoC increases. In the  $z$ -scan and time-series measurement, the CCT can change up to  $\sim 5 \mu\text{m}$  and RoC up to  $\sim 0.5$  mm.

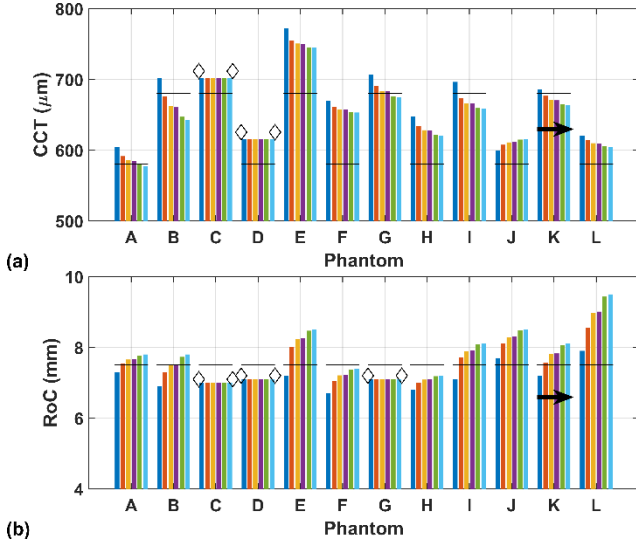


Figure 5. Interpolated (a) CCT and (b) RoC of the phantom during different stages of the measurements. The black arrow at Sample “K” shows the direction of increasing time. The diamonds show phantoms where the before or after OCT measurement failed to produce reliable thickness or RoC result.

#### IV. REFLECTIVITY MEASUREMENTS AND PROCESSING

The corneal phantom submillimeter-wave reflectivity was acquired with the quasi-optical system described in [8] and [26]. The system consists of a vector network analyzer (N5225B PNA, Keysight

Technologies) coupled to a VNA extender operating in the 220 GHz – 330 GHz band (WR3.4-VNAX, Virginia Diodes Ltd). The quasi-optics were based on a Gaussian-beam-telescope configuration with two bi-convex, custom aspheric lenses. The lenses were made of the cyclic-olefin copolymer TOPAS. In the measurement, the spherical phantom apex was co-aligned with the Gaussian beam and positioned between the Gaussian-beam waist and one confocal distance ( $z_c = \pi w_0^2 / \lambda$ ) where the beam radius of curvature approximately matches that of the phantom ( $R \approx 7.5$  mm). The phantom was mounted on linear translational stages and scanned over a  $1 \text{ mm} \times 1 \text{ mm} \times 1 \text{ mm}$  volume to identify the peak reflection position which corresponded to a curvature match between wavefront and phantom anterior surface.

The measurements include cross- and in-range scans for alignment and processing the reflectivity measurements (Figure 6). Both the corneal phantom and spherical metal reflectors were scanned in space in the output beam of the quasi-optics. The location of the maximum reflection for the phantom was considered to correspond situation when the Gaussian output beam wavefront matches with the phantom surface. The peak temporal location, identified in time domain representation of  $S_{11}$  (via the DFT), with the phantom was recorded. The metal sphere reflection that showed an  $S_{11}$  time-domain peak the at the same time as the phantom was selected as the reference  $S_{11}$  for calibration. This method assured that both the phantom and metal reflector apices were at as close positions as possible.

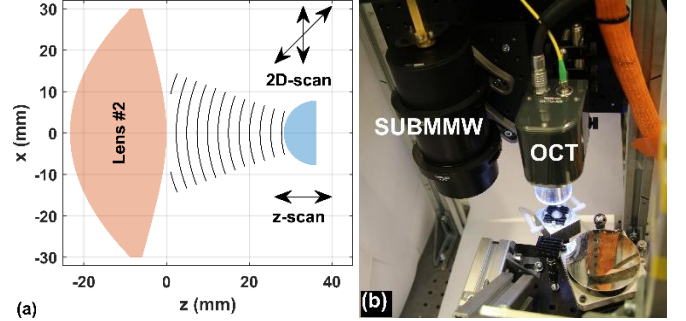


Figure 6. a) Measurement geometry: corneal phantom is located in the output Gaussian beam of the quasi-optics and it is 2D-scanned for optical-axis alignment and  $z$ -scanned for finding the optimal phase matching with the curved surface and to carry out spatial filtering. b) Photograph of the phantom located for OCT measurement. The submillimeter-wave quasi-optics is to the left in the figure. Also spherical reference reflector and planar mirrors are shown.

The reflectivity of the corneal phantom was acquired by normalizing the phantom reflection with the reference metallic sphere reflector whose radius of curvature was similar to the phantom anterior surface radius of curvature:

$$\Gamma_m = -\frac{S_{11,p}(f, z)}{S_{11,m}(f, z)} = -\frac{S_{11,p}}{S_{11,m}} \quad (1)$$

where  $S_{11,p}$  and  $S_{11,m}$  are the reflections from the phantom and the spherical reference reflector respectively and the  $(f, z)$  pairs indicate that the S-parameters were obtained in the frequency domain for a given location,  $z$ , along the optical axis. The minus sign in (1) originates from assuming that the reference sphere reflection coefficient is  $-1$ . Multiple reflections within the aspheric lenses did not allow direct measurement of  $S_{11,p}$  nor  $S_{11,m}$  and time gating and spatial filtering methods were used. The temporal and the spatial frequency relationships are described by the following windowed discrete Fourier transform relations between frequency and time domains as

$$S(t_n, z) = \frac{\sum_m w_{1,m} S(f_m, z) e^{-j2\pi f_m t_n}}{\sum_m w_{1,m}}, \quad (2)$$

$$S(f_n, z) = \frac{\sum_m w_{1,m} S(t_m, z) e^{-j2\pi t_m f_n}}{\sum_m w_{1,m}}, \quad (3)$$

$$w_{1,m} = 1 - e^{-\left(\frac{1-m}{0.28N}\right)^2} - e^{-\left(\frac{N-m}{0.28N}\right)^2}, \quad (4)$$

$$m = 1 \dots N, N = 133$$

and between the spatial-frequency and spatial domains as

$$S(f, u_{z,n}) = \frac{\sum_m w_{2,m} S(f, z_m) e^{-j2\pi z_m u_{z,n}}}{\sum_m w_{2,m}}, \quad (5)$$

$$S(f, z_n) = \frac{\sum_i w_{2,m} S(f, k_{z,m}) e^{j2\pi u_{z,m} z_n}}{\sum_m w_{2,m}}, \quad (6)$$

$$w_{2,m} = 1 - e^{-\left(\frac{1-m}{0.05N}\right)^2} - e^{-\left(\frac{N-m}{0.05N}\right)^2}, \quad (7)$$

$$m = 1 \dots N, N = 100,$$

where  $w_{1,m}$  and  $w_{2,m}$  are custom window functions chosen semi-empirically. Oscillations were quantified in the  $z$ -scan (along the quasioptical system optical axis) of the phantom and calibration targets. Equations (2), (4), (5), and (7) were used to generate the time-space ( $t_n, z$ ) and frequency-spatial frequency ( $f, k_{z,n}$ ) plots of Figure 7.

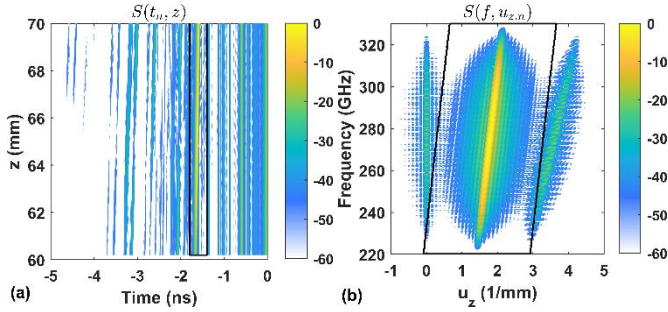


Figure 7. a) Time-domain representation of  $S_{11}$  measurement in  $z$ -scan. The rectangular area (black) indicates the location of gating window. b) Spatial-domain representation of the time-gated  $S_{11}$  measurement in  $z$ -scan. The parallelogram (black) shows the pass band of the spatial filter. The colorbar scale is in decibels.

The multiple reflections from the quasioptics in the time domain approximately occupy time from 0 to  $-5$  ns, partly overlapping with the reflection from phantom at about  $-1.65$  ns (Figure 7 (a)). Time gating reduced interference arising from reflections within the quasioptics that occur at time points displaced from the phantom reflection. Spatial filtering was used to remove oscillations that are still present in the time-gated reflections from phantom and calibration target. These oscillations were also a result of multiple reflections within the aspheric lenses whose arrival times coincided with the phantom reflection arrival times. The constant component (multiple reflections from stationary quasioptics) was separated from the first-order reflection from the moving phantom (Figure 7 (b)). Also, the second-order reflection (at  $3 \dots 4$  1/mm) from the phantom was filtered out. Similar measurement techniques have been applied in submillimeter-wave radar techniques in [17], [15], and [16].

### A. Time gating

Figure 8 shows the calibrated frequency- and time-domain reflectivity ( $S_{11}$ ) for a gelatin phantom and a metallic spherical reflector in the output of the Gaussian-beam telescope. The time-domain  $S_{11}$  was calculated with a manual discrete Fourier transform (DFT) in time window from  $-1.8$  to  $-1.4$  ns where the time/frequency bins in Equation (2) were defined for significant oversampling to avoid scalloping loss and aliasing. The reference reflector and

phantom reflections occurred at  $\sim -1.618$  ns, although the corneal phantom demonstrated noticeable variation in temporal location due to small differences in phantom geometry which impart an arrival time uncertainty. The time-domain reflections were inverse transformed back to the frequency domain, now containing the reflection from the phantom and metal reflector without the first-order reflections from the dielectric lenses.

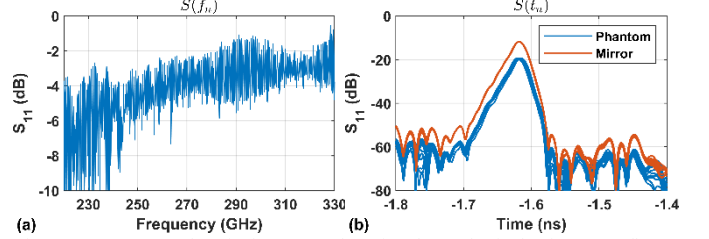


Figure 8. a) Measured  $S_{11}$  in frequency domain when spherical reference reflector is aligned with the output Gaussian beam. b) Time-domain  $S_{11}$  for all the measurements of reflectors and corneal phantoms.

### B. Spatial filtering

Each set of phantom measurements included a scan along the optical axis coincident with the apex of the phantom and reference reflector. The axial scan spanned 10 mm about the peak return location of each target/reflector. In addition to facilitating the optimal target location for the phantom in post-processing, the axial scan data was used to further filter interferences in the measured  $S_{11}$ . The scan step size was  $\Delta z = 100 \mu\text{m}$ , allowing measurement of Nyquist-sampled reflections up to the spatial frequency  $u_z = 1/\Delta z$ .

Figure 9(a) shows the midband (275 GHz)  $S_{11}$  when the spherical reflector was scanned along  $z$ -axis. The peak at  $\sim 64.3$  mm is due to approximate wavefront RoC matching at the beam subconfocal point [8]. The signal increased beyond 67 mm is evidence of a second signal maximum arising from less efficient wavefront RoC matching at the superconfocal point [8] that occurred beyond the span shown in the graph.

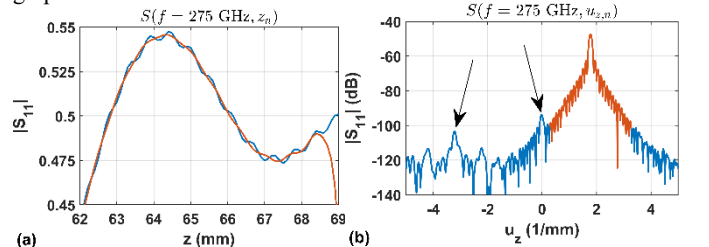


Figure 9. a) Time-gated  $S_{11}$  as function of phantom distance. The phantom was aligned at the peak location at 64.3 mm. Ripple due to interfering reflection is seen in the time-gated  $S_{11}$  (blue) but is filtered out by additional spatial filtering (red). b) Spatial-frequency domain  $S_{11}$  with the phantom reflection seen at  $1.8 \text{ mm}^{-1}$ . Interfering reflections are seen especially at  $0 \text{ mm}^{-1}$  and  $-3.2 \text{ mm}^{-1}$ .

Without the spatial filtering, a ripple with period of  $\sim 0.5$  mm is present, as shown by the blue curve in Figure 9(a). The ripple is  $\sim 47$  dB below the phantom reflection as evidenced by the spur at  $u_z = 0$  in the spatial frequency plot in Figure 9(b). Pass-band filtering of  $\pm 10$  rad/mm around the phantom reflection indicated by the red overlay in Figure 9(b) creates the smooth, clutter free  $S_{11}$  of Figure 9(a).

The reflectivity was calibrated using the time gating and spatial filtering. The normalization from (1) was applied to the data from all 12 phantoms and associated with the position of maximum phantom reflectivity. The phantom geometry deviated slightly from sample to sample, and thus the optimum  $z$  varies as well. As seen in Figure 8 (b), this produced small distance differences between the reference reflector and phantom apex for each phantom measured. The distance

uncertainty primarily perturbs the measured phase and, to compensate, the remaining linear part of the measured phase was de-embedded from the reflectivity. Figure 10 (a) and (b) show the reflection from the phantom and reflector in z-scan for phantoms “A” and “C”. The normalization and phantom reflection,  $S_{11,m}$  and  $S_{11,p}$ , were selected from the location yielding the maximum average reflectivity. The phantom and reference reflector locations are aligned in Figure 10 (a) and (b). The normalized reflection from phantom “A” is similar with that from the spherical reference reflector, whereas the normalized reflection from “C” shows deviation between the phantom and reflector contours. The deviation indicates poor phantom geometry during the measurement.

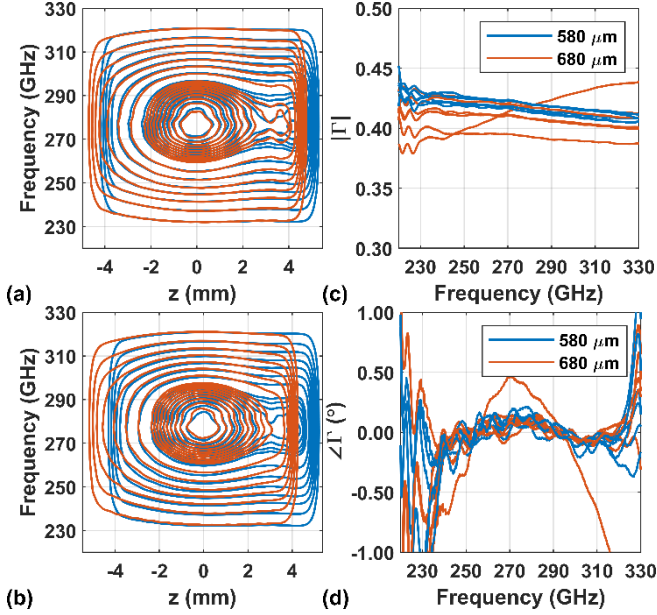


Figure 10. Time-gated and spatial-filtered  $S_{11,p}$  (red) and  $S_{11,m}$  (blue) for phantoms (a) “A” and (b) “C” during z-scans. The amplitude contour plots are normalized and offset on z-axis so that the peak is at origin. The excellent overlap in (a) shows very accurate geometric match, whereas match in (b) is less so. (c) Amplitude and (d) phase of the reflectivity of 12 phantoms. The amplitude and phase for phantom “C” is dissimilar to the rest of the phantoms.

Figure 10 (c) and (d) show the amplitude and phase of the maximum reflectivity of the phantoms. Phantom “C” was considered a poor phantom as its sphericity degraded between fabrication and mounting thus producing poor beam coupling and high measurement uncertainty. The phantom data below 240 GHz was distorted due to oscillations related to the measurement system and gating artifacts, which occur above 310 GHz as well. In the subsequent analysis, only frequencies from 240 to 310 GHz were considered. The combined time gating and spatial-domain filtering resulted in amplitude and phase clutter reduction down to  $1e-3$  and  $0.1^\circ$  peak-to-peak, respectively.

## V. PARAMETER FITTING TO CORNEAL PHANTOM

This section describes the process of fitting the corneal parameters to the measured corneal phantom reflectivity. shows a flowchart of the fitting process. The flowchart shows the arrival to the corneal phantom reflectivity,  $\Gamma$ , as is described in Section IV. The flowchart shows the subsequent parameter fitting with the particle-swarm optimization (PSO) and its dependency on the gelatin dielectric model and stratified medium model. Phantom CCT is either given directly from the OCT measurement or determined as a free parameter in PSO iteration.

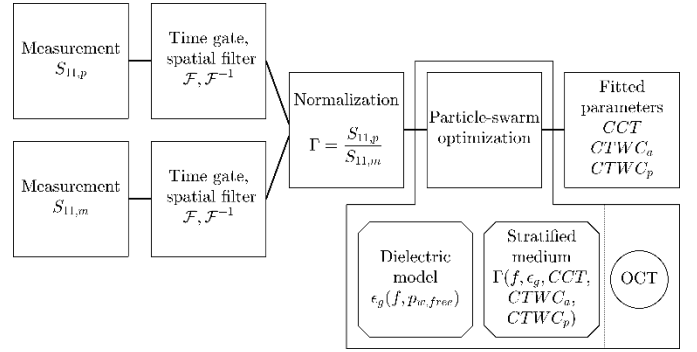


Figure 11. Flowchart of the measurement processing and parameter fit. The processing is identical for the phantom and metal reflector. The phantom reflectivity is given by the normalization after which the PSO is run to find the phantom parameters. The iteration is supported by the gelatin dielectric model and stratified medium model. Fit is carried out with and without CCT directly from the OCT.

### A. Dielectric model for gelatin hydrogel

The THz dielectric permittivity of collagen-based gelatin has been reported previously [27]. A dielectric model for the same food-grade gelatin sample used here, was introduced in [26] over the 220 – 330 GHz range. Initial experiments and data fitting with this gelatin considered the free and bound water fractions as a mixed medium following the Bruggeman’s model. The compound of water bound to gelatin molecules was termed “solid content” and demonstrated a permittivity of  $\epsilon_{sc} = 3.86 - j2.51$ . The free-water fraction followed the submillimeter-wave permittivity of water, described by the double-Debye model in [28]. The water content fractions in bulk gelatin hydrogel in [26] were measured both with submillimeter-wave setup and DSC. The free-water content was determined in gelatin hydrogel samples with four different total-water concentrations from 67 to 81 vol %. In the following determination of free-water content in the phantoms, an empirical model was needed to represent free-water contents from 0 to 100 vol %. The measured data was extrapolated at 0 to 67 vol % and 81 to 100 vol % using cubic spline interpolation for the ranges delineated by the shaded columns:

$$\begin{aligned} p_{w,free} &= 0, 26.3, 27.4, 42.2, 68.9, \text{ and } 100, \\ p_{w,total} &= 0, 67, 72, 77, 81, \text{ and } 100. \end{aligned} \quad (8)$$

The corneal phantom parameters were fit with an iterative particle-swarm algorithm [29], [30], [31]. To ensure convergence, the free-water content was interpolated with cubic interpolation to arrive at continuously differentiable free-water content from 0 to 100 vol %. MATLAB built-in function “interp1” was used with piecewise cubic Hermite interpolating polynomial (PCHIP) as the interpolation method. Figure 12 (a) shows the free-water content in gelatin hydrogel as a function of the total-water content and the dielectric model. The measurements showed consistently low free-water content from 67 to 77 vol % and a rapid increase in water content from 77 to 81 vol %. The water content of the fabricated phantom was between, 100 % water at the posterior interface (maximum) and the relative humidity of the surrounding air at the anterior surface. Time-domain simulations on water transport in the phantom indicate a linear water content profile, which was used as a baseline to fit a stratified corneal model to the experimental data. The free-water content was a second-order monotonic function decreasing towards 0 vol % and increasing towards 100 vol %. The extrapolated free-water content in hydrogel is shown with dashed line in Figure 12 (a). The dielectric permittivity of the gelatin hydrogel was defined with the Bruggeman formula:

$$p_{w,free} \frac{\epsilon_w - \epsilon_g}{\epsilon_w + 2\epsilon_g} + (1 - p_{w,free}) \frac{\epsilon_{sc} - \epsilon_g}{\epsilon_{sc} + 2\epsilon_g} = 0, \quad (9)$$

where  $\epsilon_w$  is the permittivity of pure water,  $\epsilon_{sc}$  is the permittivity of solid content (compound of water bound to gelatin) and  $p_{w,free}$  is the fraction of free water. The model converges to the permittivity of solid content at 0 vol % and to double-Debye mode of pure water at 100 vol %, as shown in Figure 12 (b).

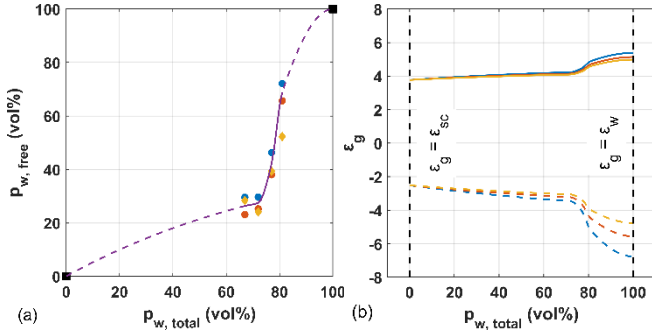


Figure 12. a) Free-water content in gelatin hydrogel determined from SUBMMW (dots) and DSC (diamonds) measurements. The free-water content model is interpolation from the measurements (from 67 to 81 vol %) and boundary conditions (squares at 0 vol % and 100 vol %). b) Permittivity of gelatin hydrogel at 220-330 GHz based on the dielectric model from [26].

### B. Stratified medium model

The reflectivity from the corneal phantom is measured through a Gaussian-beam telescope where the diverging Gaussian beam from transceiver was coupled to the corneal phantom surface via a set of aspheric lenses [8]. The corneal phantom was modeled as a stratified medium with finite layers of water and corneal tissue preceded by air and succeeded by a water half-space. When the corneal phantom surface was properly aligned with the Gaussian beam, the observed spectra was assumed to follow the stratified medium model. The local incidence angle was close to normal across the transverse beam extent. In the model, the corneal phantom was divided into constant-thickness layers where the characteristic permittivity of each layer was defined by its free-water content. The reflectivity from the phantom-water interface at the posterior surface of the cornea initiates the recursion (Equation (10)) and the reflection from successive interfaces was computed with Equation (11):

$$\Gamma_N = \rho_N = \frac{\sqrt{\epsilon_{g,N}} - \sqrt{\epsilon_w}}{\sqrt{\epsilon_{g,N}} + \sqrt{\epsilon_w}} \quad (10)$$

$$\Gamma_i = \frac{\rho_i + \Gamma_{i+1} e^{-2jk_0 \sqrt{\epsilon_{g,i}} d}}{1 + \rho_i \Gamma_{i+1} e^{-2jk_0 \sqrt{\epsilon_{g,i}} d}}, \quad i = N, N-1, \dots, 1, \quad (11)$$

where  $\epsilon_{g,i}$  is the dielectric permittivity of  $i$ th layer of gelatin hydrogel according to the model described in the previous section. A layer thickness of  $d = 10 \mu\text{m}$  was used in all stratified medium calculations. The parameter fit to corneal phantom reflectivity data was carried out with particle-swarm optimization. PSO is described in more detail in [29]. Independent OCT measurements informed the phantom thickness before and after the submillimeter-wave measurements. The gelatin hydrogel permittivity was described previously [26]: lossy “dry” material mixed with free water “mixed” Bruggeman effective medium theory.

### C. Linear Gradient Shape

The gelatin hydrogel phantom front surface was exposed to air and the back surface was exposed to liquid water at a constant  $\sim 980$  Pa pressure. This combination of environmental factors, together with the experiment duration very likely created a free water content gradient along the optical axis of the gelatin phantom. Since external, non-invasive quantification of aqueous gradients was not possible, a

hydrodynamic simulation was performed to estimate gradient shape. The simulations follow Fick’s Second Law assuming constant water diffusivity of  $1e-10 \text{ cm}^2/\text{s}$  [26], [4]. 0.58 mm and 0.68 mm thick gelatin layers were simulated by discretizing the bulk to 58/68 homogenous layers, each  $10 \mu\text{m}$  thick and the water gradient and thickness were tabulated as a function of time spanning the total experimental data acquisition duration. An example of the 0.58 mm simulated thickness time series and experimentally obtained results of the 0.58 mm thick phantom, via OCT are shown in Figure 13(a). After the initial water intake and resulting thickness increase, the thickness decays towards a steady state. This trend matches well with the OCT data represented by the  $\square$  markers. The corresponding simulated gradients for the times indicated by the markers are displayed in Figure 13(b). The water gradient initially takes on a sigmoidal-like distribution and then rapidly settles to a linear distribution.

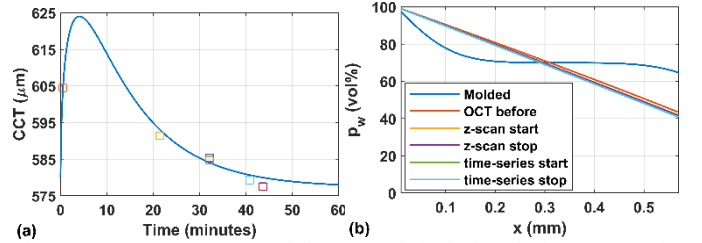


Figure 13. Water-content simulations of gelatin hydrogel phantom: a) The simulated thickness of the phantom (blue) with experimental OCT measurements (squares). b) The water-content profile at different points of time in measurements. The profile can be approximated as linear in all cases but immediately at the beginning of the simulation.

These results strongly correlate with free-water content measurements with differential scanning calorimetry (DSC) of bovine cornea [20]. Water-content gradients have also been included in analysis of submillimeter-wave spectroscopy in [4]. Based on the simulation, the water-content profile can be approximated as linear after the initial transient. This linear profile simplifies the particle-swarm optimization as it limits the water gradient degrees of freedom to two: the anterior and posterior water content values.

### D. Particle-swarm optimization

The following parameters were fit to the time/frequency, space/spatial frequency processed reflectivity:

- $\text{CTWC}_p$ : Corneal tissue water content (total water content) at the posterior surface
- $\text{CTWC}_a$ : Corneal tissue water content (total water content) at the anterior surface
- CCT: central corneal thickness

The parameter space used in PSO fitting is listed in Table I. The water content profile of the phantom was defined by its front and back water content and thickness:

$$\text{CTWC}(z) = \text{CTWC}_a(1 - \hat{z}) + \text{CTWC}_p \hat{z}, \quad (12)$$

where  $\hat{z} = z/\text{CCT}$  is the normalized depth to the phantom. The corneal phantom thickness (CCT), was either estimated by PSO or provided to the PSO algorithm as an input through the OCT measurements. The optimization penalty function was the sum of square errors over the complex plane:

$$O_i = \sum_{f_0}^{f_N} (|\Gamma_i(f_j) - \Gamma_m(f_j)|)^2, \quad (13)$$

where  $\Gamma_i(f_j)$  the theoretical complex reflectivity corresponding to  $i$ th particle in the optimization and  $\Gamma_m(f_j)$  is the processed, measured reflectivity at frequency  $f_j$ .

Table I  
PARAMETERS IN PSO FITTING ALGORITHM

PSO setup	Value	Parameter	Range
Max. # of iterations	60	CTWC <sub>p</sub> (%)	0...100
# of variables	3,4	CTWC <sub>a</sub> (%)	0...100
# of particles	101	CCT ( $\mu\text{m}$ )	200...1000
Fitting frequency (GHz)	240...310	$\Delta z$ (mm)	-4...4
$\Delta h$ ( $\mu\text{m}$ )	10		

## VI. EXPERIMENTAL RESULTS

The measured and fitted reflectivity magnitude and phase for Phantoms A – L are shown in Figure 14. The top row (Figure 14 (a) – (b)) reports results where phantom CCT was estimated from the submillimeter wave data and the bottom row (Figure 14(c) – (d)) shows fits when the OCT derived CCT was given as an input to the PSO routine. The poor fit between data and parameter estimates on phantom “C” provides additional evidence that abnormal geometry causes error in the parameter extraction procedure described in Figure 11. The fitted parameters shown in Figure 15 and the and the penalty function values are reported in Figure 15(a) and represented by the  $\circ$  marker referenced to the right-side vertical axis. The phantom order on the horizontal axes of all panels in Figure 15 was produced via sorting by increasing thickness prediction error,  $\Delta\text{CCT} = |\text{CCT}_{\text{SUBMMW}} - \text{CCT}_{\text{OCT}}|$  as reported on the left-side vertical axis Figure 15(a). The horizontal lines across each pair of bars indicate the intended fabrication thickness. In general, the penalty function values are small for the phantoms where the thickness is successfully predicted.

The fitted total-water content of the corneal phantoms is shown for both optimization cases: Figure 15(b) where the CCT is fitted as a free parameter and Figure 15(c) where OCT-derived CCT is provided as in input. The CTWC<sub>p</sub> fit returns  $\sim 100\%$  for the majority of phantoms for both the free and fixed CCT cases. The two fitting cases also result similar CTWC<sub>a</sub> values at the cornea's anterior surface for the phantoms where the CCT prediction error was low. Phantoms B, A, F, and J had the smallest differences between the PSO CCT estimations and OCT CCT measurements (Figure 15 a); accordingly, they also exhibit a good fit to a circular profile. Unsurprisingly, phantom C has the most significant error.

OCT images of phantoms “B”, “E”, and “C” are shown in Figure 16. These three represent the best, median, and worst penalty function values, respectively. Phantom “B” appears symmetric with only a change in the phantom apex height before and following submillimeter-wave measurements. The thickness error is  $\sim 5\ \mu\text{m}$  and CTWC<sub>a</sub> is 55.8 or 55.6 vol % for the case of known thickness and fit thickness, respectively. Phantom “E” has non-uniform thickness and parameter fit varies significantly with an unrealistically low anterior water content estimate. OCT images of phantom “C” confirm non-uniform morphology with significant deformation occurring throughout the measurements. Overall, the best five phantoms fitted thickness error was less than  $118\ \mu\text{m}$  ( $0.23\lambda$  in corneal tissue) and anterior water content is similar invariant in both the OCT provided CCT case and the case where CCT is estimated from submillimeter-wave reflectivity.

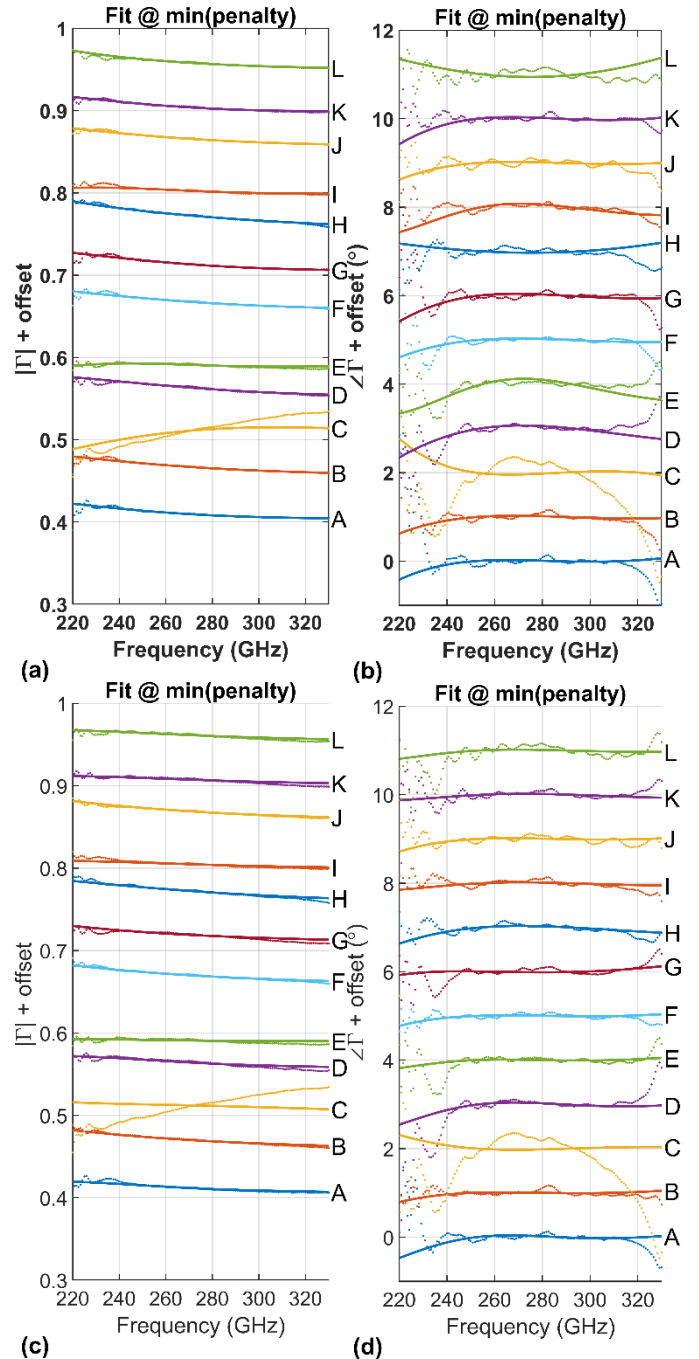


Figure 14. Measured (dots) and fitted (solid) reflectivity of all 12 phantoms. The amplitude and phase values are offset by 0.05 and  $1^\circ$  for better visibility, respectively. Offset is zero for phantom “A”. a) and b) show the results when CCT was fit and c) and d) when CCT was given from the OCT measurement.

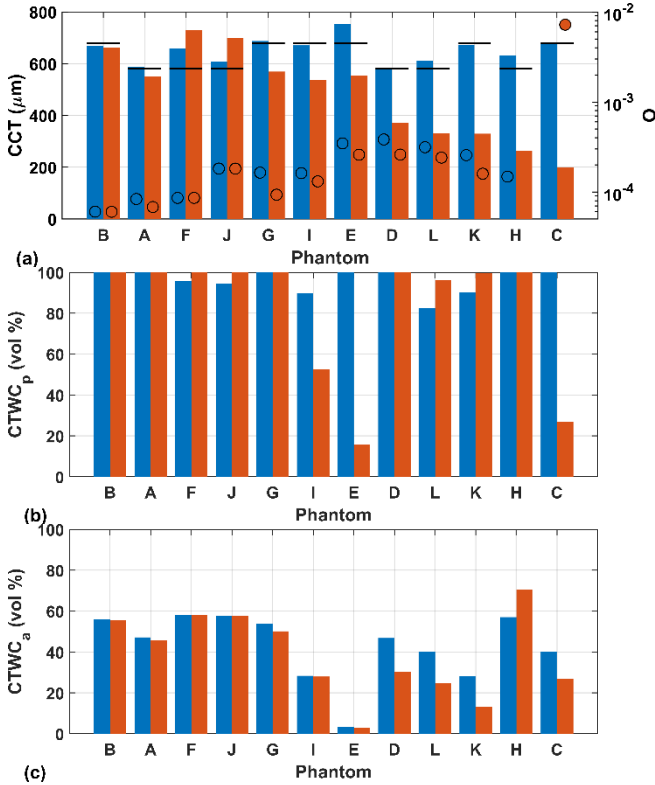


Figure 15. Results of phantom parameter fits: a) CCT, b)  $\text{CTWC}_a$ , and  $\text{CTWC}_p$ . The two cases with (blue) and without (red) OCT measurement thickness data. The horizontal black lines show the design phantom thickness. Penalty function values are shown in (a) for the fits with and without OCT input.

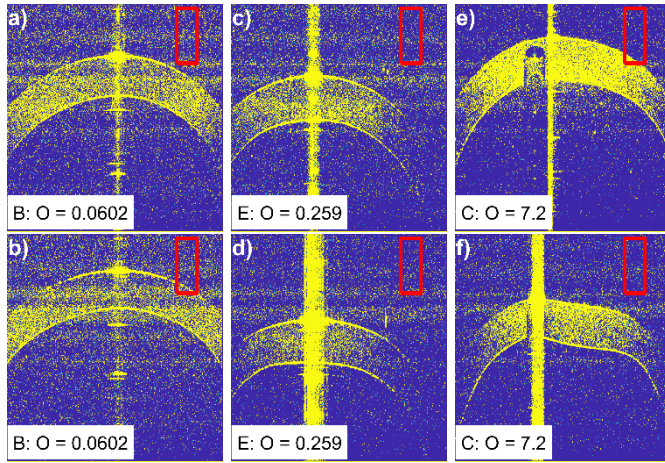


Figure 16. Examples of OCT images of corneal phantoms from the smallest penalty function value to the largest: Phantoms B (a, b), E (c, d), and C (e, f). The top row is before the submillimeter-wave measurements and bottom row is after. The red rectangle shows a 1-mm  $\times$  1-mm area in air. OCT image of phantom is exaccarated in thickness due to refractive index of gelatin (1.4).

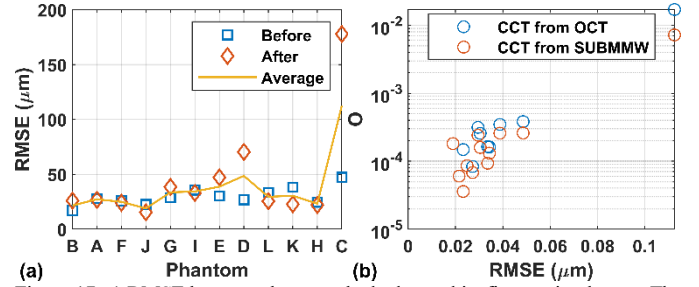


Figure 17. a) RMSE between the smoothed edge and its fit to a circular arc. The RMSE is computed for all phantoms before and after the submillimeter wave measurements. b) Optimization penalty as function of phantom RMSE. The phantoms with large deviation from spherical shape result in ill fit as well.

The correlation between sphericity parameter estimation is further explored in Figure 17. The root mean square error (RMSE) between the anterior segment edge delineated by the edge detection algorithm in the OCT image data and a best fit sphere is reported in Figure 17(a). The RMSE was computed along the vertical direction (parallel to the phantom optical axis) and the  $\square$  and  $\diamond$  markers indicate RMSE values for the pre and post submillimeter-wave acquisition times respectively. The submillimeter-wave acquisition and subsequent fit to stratified medium model is critically dependent on the sphericity of the phantom. Figure 17(b) shows the penalty function of the PSO fit to the phantom as function of RMSE: In general, poor PSO fit can be traced to significant non-sphericity detected by the OCT.

## VII. THEORETICAL ESTIMATES OF WATER CONTENT AND THICKNESS SENSITIVITY

The clutter in the experimentally observed phantom reflectivity corresponds to a signal-to-noise ratio in the range of 40-50 dB. The impact of clutter and noise on parameter extraction accuracy was explored with a Monte Carlo simulation of scenarios analogous to the experiments and experimental data analysis. The simulations follow the process shown in Figure 18. The forward analysis consisted of calculating the complex reflectivity of a phantom, which was modeled as a flat multilayer slab. The water content was distributed as a linear gradient in the thickness with a fixed total water content at the anterior surface  $\text{CTWC}_a = 40$  vol % and a varying posterior surface water content;  $\text{CTWC}_p = 70$  %,  $80$  %,  $90$  vol %. Using the mapping in Figure 12, this resulted in a free water content of  $\text{CTWC}_a = 21.6$  vol % and  $\text{CTWC}_p = 49.0, 62.2$  or  $78.8$  vol %, thus covering the span of extracted water content from the experiments. Similarly, the CCT was set to either one of two fabrication values:  $0.58$  mm or  $0.68$  mm. The slab was then discretized in layers of  $10$   $\mu\text{m}$  with the first layer properties defined by  $\text{CTWC}_a$  and the last layer properties defined by  $\text{CTWC}_p$ . Bruggeman effective media theory (Equation (9)) and stratified media theory (Equations (10-11)) were used to compute the complex reflectivity  $\Gamma$ .

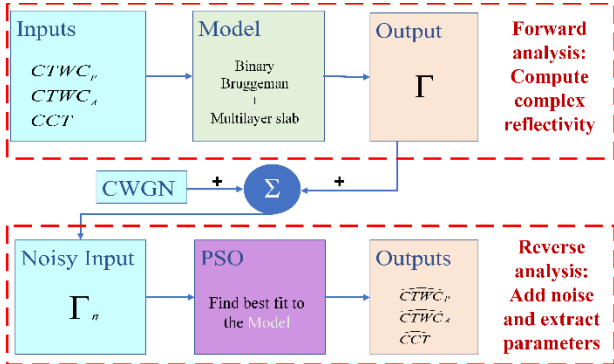


Figure 18. The complex reflectivity  $\Gamma$  is simulated through the stratified medium in the forward analysis. Noise is added and, subsequently, the thickness and the posterior and anterior water content are estimated in the reverse analysis.

Three different SNR levels were considered: 40, 50, and 60 dB, thus covering experimental values. Six combinations of phantom thickness ( $\times 2$ ) and posterior water contents ( $\times 3$ ) were simulated for each SNR ( $\times 3$ ) for a total of 18 simulations sets. Each simulation set had 60 iterations. In each iteration, complex white Gaussian noise was added to the complex reflectivity to obtain the intended SNR value. The noisy, simulated reflectivities from the forward analysis were passed through the reverse analysis where the PSO algorithm described in Section IV was used to estimate the  $CTWC_a$ ,  $CTWC_p$ , and CCT. The CCT estimation space was constrained to an interval of 100  $\mu\text{m}$  around the true value. This is justified by the fact that, in an experimental setting, one should be able estimate the phantom thickness via optical or ultrasonic pachymetry with an accuracy below 100  $\mu\text{m}$ .

The simulation results for an SNR of 50 dB are plotted in Figure 19. Especially at very high  $CTWC_p$  values, it is reasonable to assume that the reflectivity is sensitive to the water gradient slope. Namely, when the  $CTWC_p$  is high, the problem becomes non-unique, as the estimation values,  $CTWC_p$  and CCT, are linearly dependent and the estimation does not necessarily improve with an increasing finite SNR. To some extent, the slope exists for all the configurations; therefore, CCT and  $CTWC_p$  appear positively correlated with increasing correlation as the posterior water content increases. In some cases, the PSO CCT estimates tend towards parameter space boundaries. This was observable in the dark red data series with  $CTWC_p = 78 \text{ vol } \%$  and  $CCT = 680 \mu\text{m}$ . The  $CTWC_a$  estimation shows better accuracy because its estimate is dominated by the primary reflection from the air-cornea interface.

Table II reports the root mean square errors of the CCT,  $CTWC_a$ , and  $CTWC_p$  for all three considered SNRs: 40 dB, 50 dB, and 60 dB. The values in Table II, quantify the significantly smaller error in  $CTWC_a$  estimates compared with  $CTWC_p$  estimates. The  $CTWC_a$  error ranges from 0.54 % for a SNR of 40 dB to 0.05 % for a SNR of 60 dB, whereas the  $CTWC_p$  error ranges from 11.78 % to 2.88 %. The thickness estimation error was affected by both the input thickness value itself and the posterior water content (Figure 19 b).

Table II  
THEORETICAL RMSE OF THE FITTED PARAMETERS

	SNR = 40 dB	SNR = 50 dB	SNR = 60 dB
CCT ( $\mu\text{m}$ )	33.1	25.2	19.8
$CTWC_a$ (%)	0.5	0.2	0.1
$CTWC_p$ (%)	11.8	4.9	2.9

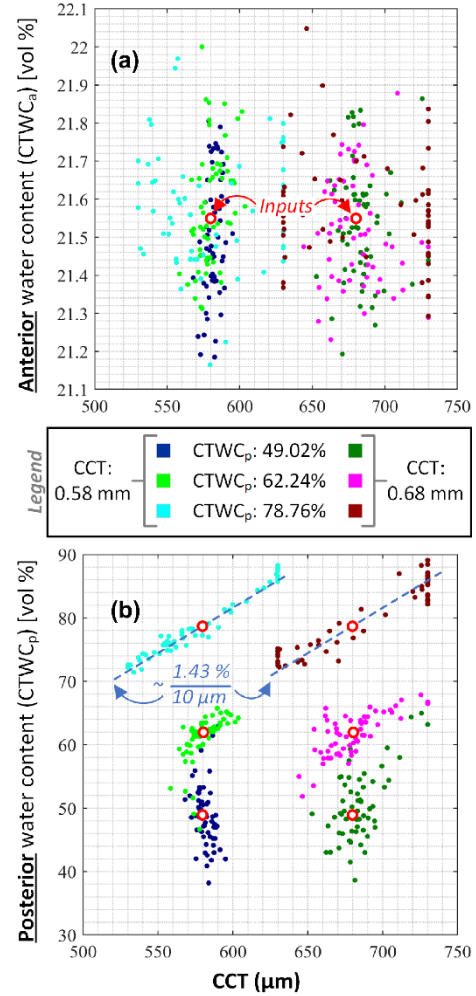


Figure 19. a) Estimated anterior water content as a function of thickness when the SNR is 50 dB b) Estimated posterior water content as a function of thickness when the SNR is 50 dB.

This analysis demonstrates contours of ambiguity for the larger posterior water content fractions. Water content-thickness pairs along these linear contours, indicated by the dotted lines with  $\sim 1.43\% / 10 \mu\text{m}$  in Figure 19(b) produce optical paths that are indistinguishable in the presence of noise and measurement error. Increases to SNR result in the region collapsing to a diagonal line and only experimentally unobtainable SNR result in the collapsing of the line to the original reference point. Additional simulations at lower frequency bands with increased penetration show a shorter and more tightly concentrated contour supporting the reduction of illumination frequency well into the millimeter wave.

## VIII. CONCLUSIONS

We have presented for the first time realistic corneal phantom with its water content and thickness determined from experimental reflectivity measured at 220-330 GHz. The low free-water content, axial dimension water-content gradients, and optically thick water backing are key characteristics necessary to make the gelatin hydrogel corneal phantom accurately mimic *in vivo* cornea. The gelatin dielectric model, derived from differential-scanning calorimetry, was used to model water-content dependent dielectric permittivity of the gelatin hydrogel. The phantom material was thoroughly characterized by simulation of water transport combined with a stratified medium theory for reflectivity: A linear gradient in water content between the posterior and anterior surfaces are well in line with the experiments.

Physically relevant water-content gradients are given after fitting to the reflectivity data. The phantom thickness was verified by an industry-standard method: Optical-coherence tomography. The reflectivity was measured by comparing the reflection from the phantom to that from a similar-sized spherical reflector. In addition, time gating and spatial-domain band-pass filtering was used to suppress the background reflection due to the dielectric quasioptics. Our method to predict the water content and thickness from submillimeter-wave reflectivity was evaluated by comparing estimated phantom water content considering a known phantom thickness and comparing the estimates to the case where thickness is a free parameter (unknown). The extracted water-content between these two cases changes little in about half of the phantoms, suggesting OCT derived adjunct data may not be necessary. Further, the OCT images reveal deviation from the intended for the phantoms that do not fit well in the submillimeter-wave model either. This is a strong indication that, given phantoms with physiologically relevant geometry, our method can accurately predict the thickness and anterior surface water content. The posterior-surface water content is more challenging to predict as the surface lies behind very lossy medium and thus contributes significantly less to the observed reflectivity.

#### ACKNOWLEDGEMENT

This work has been funded as research project AGRUM through Academy of Finland programme Radiation Detectors for Health, Safety and Security (RADDESS). This work has been carried out in MilliLab, an external laboratory of the European Space Agency.

#### References

- [1] F. Topfer and J. Oberhammer, "Millimeter-wave tissue diagnosis: The most promising fields for medical applications," *IEEE Microwave Magazine*, vol. 16, no. 4, pp. 97-113, 2015.
- [2] R. S. Singh, P. Tewari, J. L. Bourges, J. P. Hubschman, D. B. Bennett, Z. D. Taylor, H. Lee, E. R. Brown, W. S. Grundfest and M. O. Culjat, "Terahertz sensing of corneal hydration," in *2010 Annual International Conference of the IEEE Engineering in Medicine and Biology*, 2010, pp. 3021-3024.
- [3] Z. D. Taylor, R. S. Singh, D. B. Bennett, P. Tewari, C. P. Kealey, N. Bajwa, M. O. Culjat, A. Stojadinovic, H. Lee, J. Hubschman, E. R. Brown and W. S. Grundfest, "THz Medical Imaging: in vivo Hydration Sensing," *IEEE Transactions on Terahertz Science and Technology*, vol. 1, no. 1, pp. 201-219, 2011.
- [4] Q. Sun, R. I. Stantchev, J. Wang, E. P. Parrott, A. Cottenden, T. Chiu, A. T. Ahuja and E. Pickwell-MacPherson, "In vivo estimation of water diffusivity in occluded human skin using terahertz reflection spectroscopy," *Journal of Biophotonics*, vol. 12, no. 2, pp. e201800145, 2019.
- [5] D. Bennett, Z. Taylor, P. Tewari, S. Sung, A. Maccabi, R. Singh, M. Culjat, W. Grundfest, J. P. Hubschman and E. Brown, "Assessment of corneal hydration sensing in the terahertz band: in vivo results at 100 GHz," *Journal of Biomedical Optics*, vol. 17, no. 9, pp. 97008-97001, 2012.
- [6] S. Sung, S. Dabironezare, N. Llombart, S. Selvin, N. Bajwa, S. Chandra, B. Nowroozi, J. Garritano, J. Goell, A. Li, S. X. Deng, E. Brown, W. S. Grundfest and Z. D. Taylor, "Optical system design for noncontact, normal incidence, THz imaging of in vivo human cornea," *IEEE Transactions on Terahertz Science and Technology*, vol. 8, no. 1, pp. 1-12, 2018.
- [7] S. Sung, S. Selvin, N. Bajwa, S. Chandra, B. Nowroozi, J. Garritano, J. Goell, A. D. Li, S. X. Deng, E. R. Brown, W. S. Grundfest and Z. D. Taylor, "THz Imaging System for in vivo Human Cornea," *IEEE Transactions on Terahertz Science and Technology*, vol. 8, no. 1, pp. 27-37, 2018.
- [8] A. Tamminen, S. -V. Pälli, J. Ala-Laurinaho, M. Salkola, A. V. Räisänen and Z. D. Taylor, "Quasioptical System for Corneal Sensing at 220–330 GHz: Design, Evaluation, and Ex Vivo Cornea Parameter Extraction," *IEEE Transactions on Terahertz Science and Technology*, vol. 11, no. 2, pp. 135-149, 2021.
- [9] A. Joshi, D. B. Bennett and O. M. Stafsudd, "Monitoring corneal hydration with a mid-infrared (IR) laser," *The Ocular Surface*, vol. 13, no. 1, pp. 43-46, 2015.
- [10] L. Ke, N. Zhang, W. Qing Yang Steve, G. Sergey, A. Abdelaziem, Z. Liu, T. Erica Pei Wen, J. S. Mehta and Y. Liu, "In vivo Sensing of Rabbit Cornea by Terahertz Technology," *Journal of Biophotonics*, pp. e202100130, 2021.
- [11] A. Chen, A. Virk, Z. Harris, A. Abazari, R. Honkanen and M. H. Arbab, "Non-contact terahertz spectroscopic measurement of the intraocular pressure through corneal hydration mapping," *Biomedical Optics Express*, vol. 12, no. 6, pp. 3438-3449, 2021.
- [12] A. A. Angeluts, A. V. Balakin, M. D. Mishchenko, I. A. Ozheredov, M. N. Prokopchuk, T. N. Saphonova and A. P. Shkurinov, "Application of THz reflectometry to eye cornea hydration measurements," in *2016 41st International Conference on Infrared, Millimeter, and Terahertz Waves (IRMMW-THz)*, 2016, pp. 1-2.
- [13] I. Ozheredov, M. Prokopchuk, M. Mischenko, T. Safonova, P. Solyankin, A. Larichev, A. Angeluts, A. Balakin and A. Shkurinov, "In vivo THz sensing of the cornea of the eye," *Laser Physics Letters*, vol. 15, no. 5, pp. 055601, 2018.
- [14] A. Chen, O. B. Osman, Z. B. Harris, A. Abazri, R. Honkanen and M. H. Arbab, "Investigation of water diffusion dynamics in corneal phantoms using terahertz time-domain spectroscopy," *Biomedical Optics Express*, vol. 11, no. 3, pp. 1284-1297, 2020.
- [15] A. Murk, R. Wylde, R. Spurrett, P. Fürholz and N. Kämpfer, "Blackbody calibration targets with ultralow reflectivity at submillimeter wavelengths," in *4th ESA Workshop on Millimetre-Wave Technology and Applications, the 8th Topical Symposium on Millimeter Waves - TSMMW2006, the 7th MINT Millimeter-Wave International Symposium - MINT-MIS2006*, 2006, pp. 359-364.
- [16] E. F. Knott, J. F. Schaeffer and M. T. Tulley, *Radar Cross Section*. 2004.
- [17] A. Tamminen, A. Lonnqvist, J. Mallat and A. V. Raisanen, "Monostatic Reflectivity and Transmittance of Radar Absorbing

Materials at 650 GHz," *IEEE Transactions on Microwave Theory and Techniques*, vol. 56, no. 3, pp. 632-637, 2008.

[18] E. R. Brown, O. B. McMahon, T. J. Murphy, G. G. Hogan, G. D. Daniels and G. Hover, "Wide-band radiometry for remote sensing of oil films on water," *IEEE Transactions on Microwave Theory and Techniques*, vol. 46, no. 12, pp. 1989-1996, 1998.

[19] S. J. Orfanidis, *Electromagnetic Waves and Antennas*. 2003.

[20] J. A. Castoro, A. A. Bettelheim and F. A. Bettelheim, "Water gradients across bovine cornea." *Investigative Ophthalmology & Visual Science*, vol. 29, no. 6, pp. 963-968, 1988.

[21] Z. D. Taylor, J. Garritano, S. Sung, N. Bajwa, D. B. Bennett, B. Nowroozi, P. Tewari, J. Sayre, J. Hubschman and S. Deng, "THz and mm-wave sensing of corneal tissue water content: electromagnetic modeling and analysis," *IEEE Transactions on Terahertz Science and Technology*, vol. 5, no. 2, pp. 170-183, 2015.

[22] Z. D. Taylor, J. Garritano, S. Sung, N. Bajwa, D. B. Bennett, B. Nowroozi, P. Tewari, J. W. Sayre, J. Hubschman and S. X. Deng, "THz and mm-wave sensing of corneal tissue water content: in vivo sensing and imaging results," *IEEE Transactions on Terahertz Science and Technology*, vol. 5, no. 2, pp. 184-196, 2015.

[23] B. H. Walker, *Optical Design for Visual Systems*. 2000.

[24] T. Zhang, A. Elazab, X. Wang, F. Jia, J. Wu, G. Li and Q. Hu, "A Novel Technique for Robust and Fast Segmentation of Corneal Layer Interfaces Based on Spectral-Domain Optical Coherence Tomography Imaging," *IEEE Access*, vol. 5, pp. 10352-10363, 2017.

[25] J. Ø Hjortdal, L. Erdmann and T. Bek, "Fourier analysis of video-keratographic data. A tool for separation of spherical, regular astigmatic and irregular astigmatic corneal power components," *Ophthalmic and Physiological Optics*, vol. 15, no. 3, pp. 171-185, 1995.

[26] A. Tamminen, M. Baggio, I. Nefedova, Q. Sun, J. Anttila, J. Ala-laurinaho, E. Brown, V. Wallace, E. Macpherson, T. Maloney, M. Salkola, S. Deng and Z. Taylor, "Submillimeter-wave permittivity measurements of bound water in collagen hydrogels via frequency domain spectroscopy," *IEEE Transactions on Terahertz Science and Technology*, pp. 1, 2021.

[27] C. Reid, *Spectroscopic Methods for Medical Diagnosis at Terahertz Wavelengths*, UCL (University College London), 2009.

[28] J. T. Kindt and C. A. Schmuttenmaer, "Far-infrared dielectric properties of polar liquids probed by femtosecond terahertz pulse spectroscopy," *The Journal of Physical Chemistry*, vol. 100, no. 24, pp. 10373-10379, 1996.

[29] J. Kennedy and R. Eberhart, "Particle swarm optimization," in *Proceedings of ICNN'95-International Conference on Neural Networks*, 1995, pp. 1942-1948.

[30] Y. Shi and R. C. Eberhart, "Empirical study of particle swarm optimization," in *Proceedings of the 1999 Congress on Evolutionary Computation-CEC99 (Cat. no. 99TH8406)*, 1999, pp. 1945-1950.

[31] F. van den Bergh and A. P. Engelbrecht, "A Cooperative approach to particle swarm optimization," *IEEE Transactions on Evolutionary Computation*, vol. 8, no. 3, pp. 225-239, 2004.